Persistent Scatterer InSAR: A comparison of methodologies based on a model of temporal deformation vs. spatial correlation selection criteria

Joaquim J. Sousa [a,b,*], Andrew J. Hooper [c], Ramon F. Hanssen [c], Luisa C. Bastos [d,e], Antonio M. Ruiz [e,f]

[a] *Escola de Ciências e Tecnologia, Universidade de Trás-os-Montes e Alto Douro, Vila Real, Portugal*
[b] *Centro de Geologia da Universidade do Porto, Portugal*
[c] *Institute of Earth Observation and Space Systems, Delft University of Technology, Delft, The Netherlands*
[d] *Observatório Astronómico, Faculdade de Ciência da Universidade do Porto, Portugal*
[e] *Department of Geosciences, Environment and Spatial Planning, Faculty of Science, University of Porto, Portugal*
[f] *Departamento de Ingeniería Cartográfica, Geodésica y Fotogrametría, Universidad de Jaén, Jaén, Spain*

ARTICLE INFO

ABSTRACT

In this paper, two Persistent Scatterer Interferometry (PSI) methodologies are compared in order to further understand their potential in the detection of surface deformation. A comparison of these two algorithms is a comparison of the two classes of PSI techniques available: coherence estimation based on a temporal model of deformation (represented by DePSI) and coherence estimation based on spatial correlation (represented by StaMPS).

Despite the similarity between the results obtained from the application of the two independent PSI methodologies, significant differences in PS density and distribution were detected, motivating a comparative study between both techniques. We analyze which approach might be more appropriate for studying specific areas/environments, which is helpful in evaluating the benefits that could be derived from an integration of the two methodologies. Several experiments are performed to assess the sensitivity of both PSI approaches to different parameter settings and circumstances. The most significant differences in the processing chain of both procedures are then investigated. We apply both methodologies to the Granada Basin area (southern Spain) and realize that coherence does not improve significantly as function of the methodology applied. If oversampling is implemented in the StaMPS processing chain, the PS density increases so that the density in the urbanized areas is similar to the results provided by DePSI but in all the remaining covers the density is significantly higher. The general results provided by both approaches are very similar in the relative deformations estimated.

© 2011 Elsevier Inc. All rights reserved.

1. Introduction

Radar interferometry (InSAR) has matured to become a widely used geodetic technique for measuring deformation of the Earth's surface. There are two main characteristics which make this technique attractive to the scientific community. The first is that it gives a high resolution two-dimensional representation of the deformation over 10s to 100s of kilometers. The second is the high accuracy of the deformation that can be measured. The accuracy depends chiefly on variation in atmospheric conditions; the variable water vapor distribution related to the turbulent character of the atmosphere creates an interferometric phase contribution (Hanssen, 2001). For single interferograms, this atmospheric phase screen (APS) cannot easily be removed and therefore the accuracy of measuring small deformations is significantly reduced. The challenge is to separate the desired signal from the sum of all contributions to the phase. For terrain displacement studies, temporal decorrelation can be considered a random noise source while errors in the digital elevation model (DEM) used to remove the topographic phase, orbital errors, and atmospheric changes will introduce a spatially systematic phase trend.

Until recently, a large proportion of InSAR application results were achieved by analyzing single interferograms derived from a single pair of SAR images. In the late 1990s it was noted that some radar targets maintain stable backscattering characteristics for a period of months or years or even decades (Usai, 1997; Usai & Hanssen, 1997). This provided the basis for further exploitation of existing SAR scene archives using Multi-temporal InSAR techniques (MT-InSAR), involving the processing of multiple acquisitions in time, to overcome conventional InSAR limitations: temporal and geometric decorrelation, and atmospheric inhomogeneities (Ferretti et al., 1999, 2001). The main concept behind PSI technique lies on the identification of single targets (called Persistent Scatterers, PS) that are coherent over long time intervals and for wide look-angle variations (Ferretti et al., 2000, 2001). The signal received for these targets varies little as the other scatterers move around, and any motion of the scatterer can be

* Corresponding author at: Quinta de Prados Apartado 1013, 5001-801 Vila Real, Portugal. Fax: +351 259350356.
E-mail addresses: jjsousa@utad.pt, jjmsousa@gmail.com (J.J. Sousa).

readily measured by the phase of the radar echo. In fact, when the dimension of the PS is smaller than the resolution cell, the coherence is good even for image pairs taken with baselines greater than the decorrelation length. On those pixels, sub-meter DEM accuracy and millimetric terrain motion detection can be achieved (see e.g. Ketelaar, 2008; Hooper, 2006), even if the coherence is low in the surrounding areas. Reliable elevation and deformation measurements can, then, be obtained on this subset of image pixels that can be used as a 'natural geodetic network'.

In this paper we compare two persistent scatterer methods representing the two different approaches: those that select pixels based mainly on their phase variation in time (e.g., Ferretti et al., 2001; Kampes, 2005; Ketelaar, 2008) and those that use mainly correlation of their phase in space (Hooper et al., 2004; van der Kooij et al., 2006). We apply DePSI (Delft PSI processing package), belonging to the former group and StaMPS (Stanford Method for Persistent Scatterers), belonging to the last group, to the same data set. Detailed descriptions of these two PSI methodologies can be found in Hooper et al. (2007), Kampes (2005), Ketelaar (2008), and Sousa (2009). Both PSI methodologies provide broadly similar results (Sousa et al., 2010a); however there are some differences, mainly concerning PS density and location. In this work we investigate all the significant differences between both implementations.

2. Setting of the study area

The study area, the Granada Basin and its surroundings, is located in southern Spain around the western and southern flanks of Sierra Nevada. From a geological standpoint, these zones are part of the Alpujárride and Nevado–Filábride complexes within the Internal Zone of the Betic Cordillera, which are filled with postorogenic deposits of Neogene to Quaternary age. The region was formed during the Alpine orogeny and is affected by a complex geologic evolution (Galindo-Zaldívar et al., 1993; Sanz de Galdeano & Vera, 1992). The Granada basin occupies the central sector of the Betic Cordillera, one of the most seismically-active areas in the Iberian Peninsula, accompanied by significant active tectonics. Granada is the most populated city of the central Betic Cordillera.

3. Satellite datasets

This work is based on a set of ERS-1/2 and Envisat SAR images from descending and ascending satellite tracks, covering the period from December 1993 to July 2006. In the case of ERS acquisitions, only the scenes acquired until the end of 2000 have been included in the processing in order to avoid high Doppler values due to the failures of the ERS-2 gyroscopes.

The ERS and Envisat tracks that cover the Granada Basin area are listed in Table. 1. Each track has been processed using interferometric combinations that refer to a common master. The master scene acquisitions have been selected based on stack coherence (see Section 5.1). Tables 2 and 3 indicate the sets of ERS and Envisat images used in this project. Each image covers 100 by 100 km^2.

Table 1
The four ERS/Envisat tracks that cover the Granada Basin area. The master has been selected based on stack coherence.

Sensor	Track	Frame	Mode	No. scenes	Master
ERS	280	2859	Dec	29	13.07.1997
ERS	187	737	Asc	6	*
Envisat	280	2859	Desc	17	*
Envisat	187	737	Asc	22	15.02.2004

* Number of scenes insufficient for PSI processing.

Table 2
ERS data for the Granada Basin area (track 280; frame 2859). Parameters are relative to the master acquisition, orbit 11657, acquired on 13-JUL-1997 10:56 AM (UTC).

#	Acq. date	Orbit	Sensor	$B_\perp$(m)	f_{dc}(Hz)
1	02-DEC-1993	12449	ERS1	920	385
2	03-JUN-1995	20308	ERS1	134	405
3	04-APR-1999	20675	ERS2	211	137
4	04-MAY-1997	10655	ERS2	−225	126
5	06-AUG-2000	27689	ERS2	269	−372
6	06-SEP-1998	17669	ERS2	180	153
7	08-FEB-1998	14663	ERS2	−141	109
8	09-JAN-2000	24683	ERS2	−36	163
9	12-AUG-1995	21310	ERS1	270	403
10	13-AUG-1995	1637	ERS2	208	120
11	**13-JUL-1997**	**11657**	**ERS2**	**0**	**123**
12	13-JUN-1999	21677	ERS2	−460	165
13	15-DEC-1996	8651	ERS2	−179	189
14	15-OCT-2000	28691	ERS2	583	−62
15	17-JUL-1999	41851	ERS1	811	407
16	18-MAY-1996	25318	ERS1	279	378
17	19-MAY-1996	5645	ERS2	198	135
18	21-AUG-1999	42352	ERS1	1446	408
19	21-OCT-1995	22312	ERS1	902	331
20	22-AUG-1999	22679	ERS2	1140	173
21	22-OCT-1995	2639	ERS2	1031	95
22	24-DEC-2000	29693	ERS2	−325	−52
23	25-MAR-1995	19306	ERS1	−1040	384
24	28-JUN-1998	16667	ERS2	−703	158
25	28-MAY-2000	26687	ERS2	923	−285
26	30-MAR-1997	10154	ERS2	409	148
27	30-OCT-1999	43354	ERS1	805	404
28	31-DEC-1995	3641	ERS2	313	170
29	31-OCT-1999	23681	ERS2	485	88

The number of interferograms is limited to 28 for ERS data and 21 for Envisat data. All 28 ERS interferograms are generated with a master image, acquired on 17 July, 1997 while Envisat interferograms are generated with a master image acquired on 15 February, 2004.

4. Mathematical modeling

Observed interferometric phase measurements are affected by the imaging geometry, topography, atmospheric propagation and scatterer displacement or deformation. In time-series InSAR, we deal with the problem of estimating a time-series of surface deformation from a series of interferograms. Hence, the interferometric phase of a pixel

Table 3
Envisat data for the Granada Basin area (track 187; frame 737). Parameters are relative to the master acquisition, orbit 10261, acquired on 15-FEB-2004 10:01 PM (UTC).

#	Acq. date	Orbit	Sensor	$B_\perp$(m)	f_{dc}(Hz)
1	13-OCT-2002	3247	ASAR	−104	−555
2	17-NOV-2002	3748	ASAR	−402	−568
3	11-MAY-2003	6253	ASAR	607	−420
4	20-JUL-2003	7255	ASAR	−62	−486
5	24-AUG-2003	7756	ASAR	−59	−574
6	28-SEP-2003	8257	ASAR	1041	−593
7	07-DEC-2003	9259	ASAR	194	−568
8	11-JAN-2004	9760	ASAR	280	−538
9	**15-FEB-2004**	**10261**	**ASAR**	**0**	**−540**
10	25-APR-2004	11263	ASAR	−256	−532
11	04-JUL-2004	12265	ASAR	634	−545
12	08-AUG-2004	12766	ASAR	568	−573
13	12-SEP-2004	13267	ASAR	200	−543
14	17-OCT-2004	13768	ASAR	−849	−544
15	30-JAN-2005	15271	ASAR	−51	−541
16	10-APR-2005	16273	ASAR	−318	−553
17	15-MAY-2005	16774	ASAR	−164	−540
18	28-AUG-2005	18277	ASAR	388	−550
19	06-NOV-2005	19279	ASAR	−225	−513
20	19-FEB-2006	20782	ASAR	660	−520
21	26-MAR-2006	21283	ASAR	1027	−508
22	09-JUL-2006	22786	ASAR	−886	−507

(φ_{int}) in a differential interferogram can be represented by (Hooper et al., 2007):

$$\varphi_{int} = \varphi_{defo} + \Delta\varphi_{\varepsilon} + \Delta\varphi_{atm} + \Delta\varphi_{orb} + \varphi_n \qquad (1)$$

where φ_{defo} represents the phase due to deformation, $\Delta\varphi_{\varepsilon}$ refers to the error introduced by using imprecise topographic information, φ_{orb} refers to the error introduced due to the use of imprecise orbits in mapping the contributions of Earth's ellipsoidal surface, φ_{atm} corresponds to the difference in atmospheric propagation times between the two acquisition used to form the interferogram and φ_n represents the phase noise due to the scattering background and other uncorrelated noise terms.

In PSI, our primary signal of interest is the return from the dominant scatterer in the resolution element. The echoes from the dimmer distributed scatterers in a pixel is also commonly referred to as "clutter" and contributes to φ_n. Signal-to-clutter ratio (SCR) defined as the ratio between the reflected energy from the dominant scatterer to that of the reflected energy from the rest of the resolution element is a measure often used to indicate the strength of the dominant scatterer in SAR pixels. High SCR (>8) pixels exhibit low interferometric phase variation (<0.25 rad) and vice versa.

PSI frameworks are a collection of spatial and temporal filtering routines that allow us to estimate each of the phase components represented in Eq. (1) by assuming a spectral structure. Section 5.2 describes the two methods used in this work.

5. Methods

5.1. Interferometric processing

Both PSI procedures used in this study make use of Delft Object-oriented Radar Interferometric Software (DORIS) (Kampes & Usai, 1999) for the interferometric processing. The key steps of interferometric processing summarized in section 1 of Figs. 1 and 2 are explained in the next sub-sections.

5.1.1. Master selection

A stack of differential interferograms coregistered to a selected master scene is the input to the PSI processing in both approaches. For N + 1 SAR acquisitions, N independent interferometric combinations between two images can be formed. The master is selected in such a way to maximize the (predicted) total coherence of the interferometric stack, based on the perpendicular baseline, temporal baseline, and the mean Doppler centroid frequency difference (Zebker & Villasenor, 1992). In short, the master scene is chosen from the available SAR images on the basis of favorable geometry related to all other images, high coherence and possibly minimum atmospheric disturbances.

5.1.2. Oversampling and coregistration

In DePSI, after reading the SLC scenes, the SAR images are oversampled by a factor of 2 (both range and azimuth directions) before the coregistration. This step is performed to avoid aliasing in the complex multiplication of the SAR images.

The oversampled images and the precise orbits (Doornbos & Scharro, 2004; Scharroo & Visser, 1998) are the input for the coregistration of the master and the slave image. This step is fundamental in interferogram generation, as it ensures that each ground target contributes to the same (range, azimuth) pixel in both the master and the slave image. For the estimation of an accurate coregistration polynomial, the coregistration windows are evenly distributed over the area of interest. Especially in rural areas that are affected by temporal decorrelation, a proper choice of coregistration windows is required.

In StaMPS oversampling is not applied and the coregistration procedure is also different. In order to avoid decorrelation problems in the case of large temporal and spatial baselines, offsets in position are estimated for each coregistration window between pairs of images with good correlation. The function that maps the master image to each other image is then estimated by weighted least-squares inversion (Hooper et al., 2007).

In both procedures, once the mapping functions are estimated, each image is resampled to the master coordinate system, using a 12 point raised cosine interpolation kernel. Then a raw interferogram is formed by differentiating the phase of each image to the phase of the master.

5.1.3. Differential interferogram computation

The interferogram is computed by complex multiplication of the master image and the resampled slave image observations. A reference Digital Elevation Model (DEM) and precise orbits data are used as input to obtain the differential interferograms. The interferometric phase component that is induced by topography is largely eliminated using the differential technique, see, e.g. (Bamler & Hartl, 1998; Burgmann et al., 2000). After the Shuttle Radar Topography Mission (SRTM), a DEM of sufficient precision is readily available for practically any area of the world between −57° and 60° latitude (Suchandt et al., 2001).

5.2. PS processing

5.2.1. DePSI

To initiate the DePSI algorithm, a first set of PS candidates (PSC) is selected (Fig. 1). These PSs should preferably have stable phase behavior in time. Because the observed wrapped interferometric phases do not enable the identification of stable points, and the computational limitations due to the initial high amount of pixels to be tested, approximation methods are used. One option is to use the scatterer's intensity as a proxy. Although it is the phase stability of a pixel that defines a PS pixel, there is a statistical relationship between amplitude stability and phase stability, which makes consideration of amplitude useful for reducing the initial number of pixels for phase analysis. The amplitude dispersion index is defined by Ferretti et al. (2001) as:

$$D_A = \frac{\sigma_A}{\mu_A} \cong \sigma_{\varphi} \qquad (2)$$

where σ_A and μ_A are, respectively, the standard deviation and the mean of a series of amplitude values. Ferretti et al. (2001) show that for a constant signal and high signal to noise ratio (SNR), $D_A \approx \sigma_{\varphi}$, where σ_{φ} is the phase standard deviation. Nevertheless, prior to this initial selection, a digital elevation model (DEM) will be used to remove most of the topographic phase signature from the interferograms. A network is formed between the selected PSC, which enable calculation of the topographic height and displacement of a PS per epoch relative to a chosen reference point (RP). Various models may be used (Leijen & Hanssen, 2007). However the application of a specific model should be tuned to a priori knowledge about the deformation development in space and time. Without any a priori knowledge about deformation, a linear deformation mechanism is usually assumed. First, the parameters of interest and ambiguities are estimated for the arcs using Integer Least Square approach. These parameters can then be spatially unwrapped, with respect to an arbitrary RP, if possible, located in a stable area. PSC that can be tested or experience ambiguities not fitting in the unwrapped network are rejected as PS and not taken into account in further processing steps. A smaller set of PS remains to which filters are applied for the separation of atmospheric phase. The atmospheric phase screen (APS) of the interferogram is computed using a geostatistical interpolation
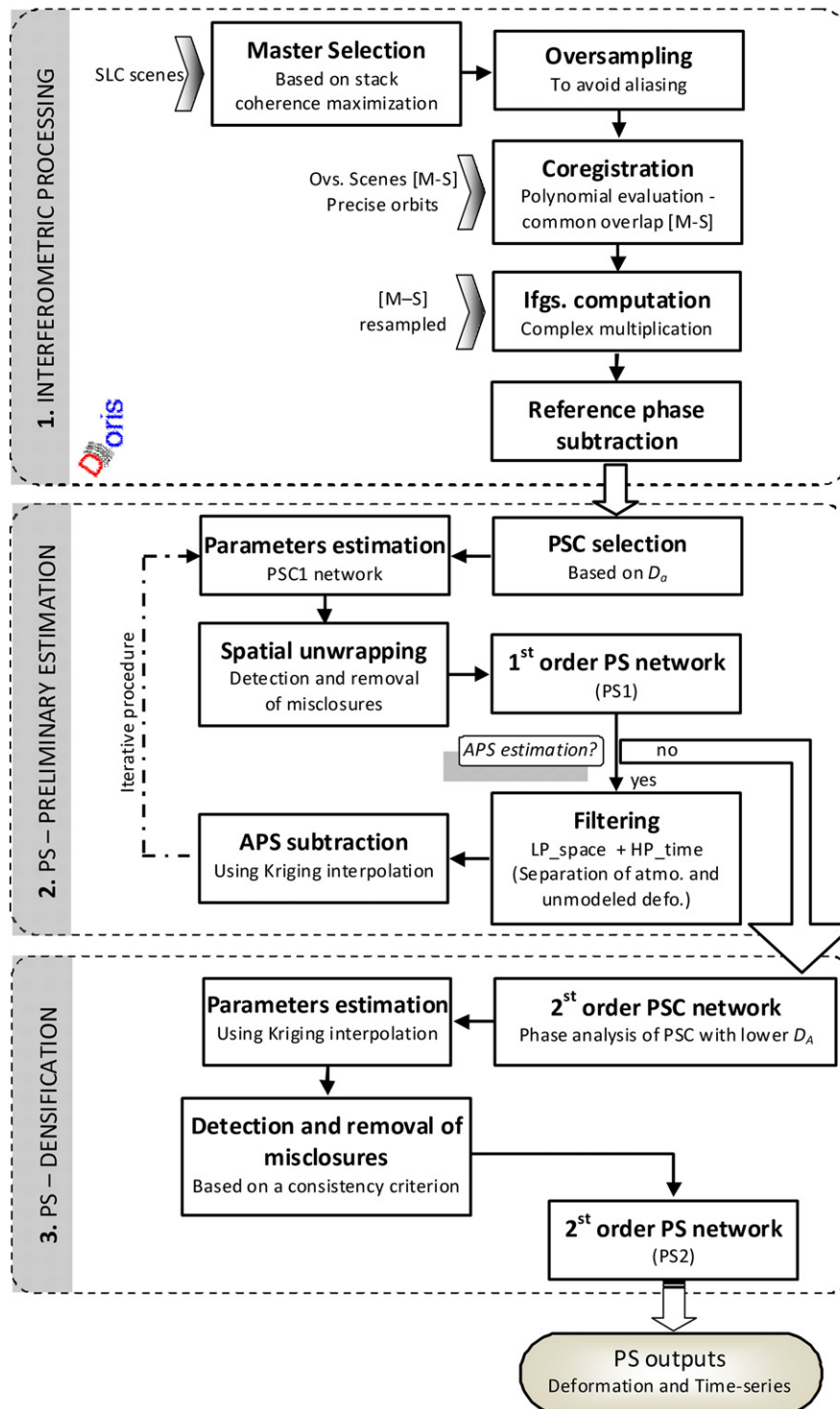
Fig. 1. Flow diagram of the DePSI processing chain.

method, which is sequentially subtracted from differential phase of the PSC. Processing steps starting from forming the network until spatial unwrapping the arcs will be performed, again using the phases corrected for the atmosphere.

Finally (section 3 of Fig. 1) after the subtraction of the atmospheric phase contribution estimated from the first order network, a further densification step is performed by the analysis of the phase history of PSC with a lower normalized amplitude dispersion. Parameter estimation is performed for each candidate (now called PS Potential — PSP)

with respect to the three closest accepted PS (belonged to the 1st order network). Again, these PSP are checked on their consistency. When at least two of the three estimated arcs are in agreement, the PSP is stored as PS. After ambiguity and parameter estimation per arc, the parameters of interests are relative in space. So, they should be spatially integrated with respect to a single reference point (reference PS) in order to obtain absolute values. Due to noise and model imperfections, residuals will be present after integration. The unwrapping errors can be identified and rejected using the spatial network. Arcs with a questionable precision
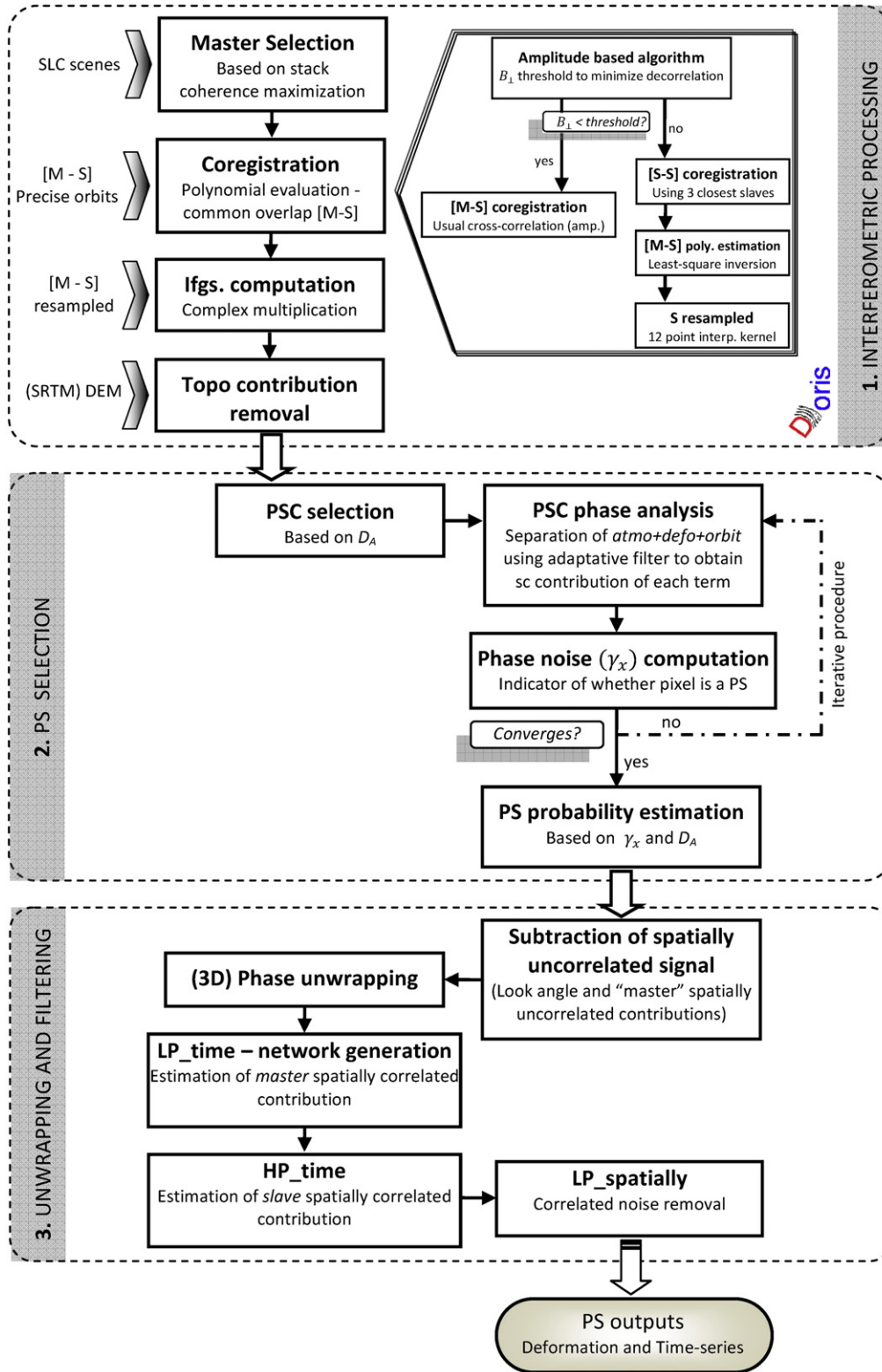
Fig. 2. Flow diagram of the StaMPS processing chain.

are rejected. This precision can be deduced from, e.g., low temporal ensemble coherence or large least-squares residues. The measure of the variation of the residual phase for a pixel (x, y) is defined as:

$$\hat{\gamma}_{x,y} = \frac{1}{N} \sum_{k=1}^{N} e^{\left(j \cdot \varphi_{error_{x,y}} \right)} \qquad (3)$$

where $\hat{\gamma}$ resembles the estimate of the ensemble coherence, N is the total amount of interferograms and j is the imaginary number. The residual, $\varphi_{error_{x,y}}$, is the difference between the modeled and observed phases at location (x, y) in the observed interferogram.

Assuming that all ambiguities are estimated correctly, the integration with respect to the RP can be carried out simply by path integration of temporally unwrapped phases without residues. The
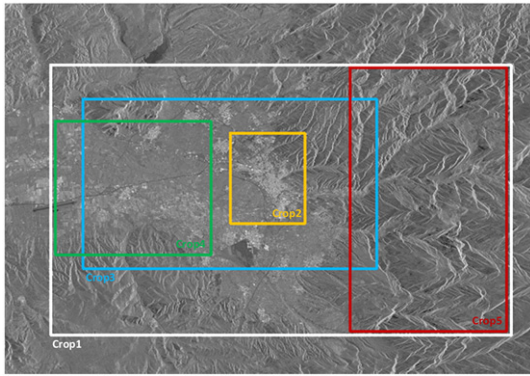
Fig. 3. Different crops used to test the DePSI and StaMPS coregistration procedures. Each crop covers a different area. (Crop1) Crop covering the major part of Granada City neighborhood (size 36×22 km^2); (Crop2) crop covering (mainly) urban area (size $\sim 6.4 \times 6.8$ km^2); (Crop3) crop covering mixed areas (urban and rural — size $\sim 23 \times 14$ km^2); (Crop4) Crop covering (almost) rural areas (size $\sim 13 \times 9$ km^2) and (Crop5) crop covering mountain area (size $\sim 11.3 \times 21.3$ km^2).

final set of PS is the union of PS1 and PS2, resulting from first and second order networks, respectively. For this final set of points, the topographic height (i.e., subtracted topography plus estimated height residual), deformation parameters, atmospheric phase, and residual phase (assumed to represent unmodeled deformation) are known relative to a single reference point.

5.2.2. StaMPS

StaMPS also uses the statistical relationship between amplitude stability and phase stability (Eq. (2)) that makes consideration of amplitude useful for reducing the initial number of pixels for phase analysis; however, the threshold value used is higher, typically in the region of 0.4, which leads to most of the selected pixels not being PS pixels. This is a very liberal threshold compared to that typically suggested for PS selection (Ferretti et al., 2001) and primarily eliminates areas over water and heavily decorrelated pixels in vegetated areas. This candidate selection stage is purely optional, but often decreases the processing time and memory requirements by a factor of ten.

Having selected a subset of pixels as initial candidates (PSC), phase stability for each of them is estimated using phase analysis. The phase stability is analyzed under the assumption that deformation is spatially correlated. Obviously, signal associated with isolated movement of individual bright scatterers may be missed and considered as noise. Again, only the fractional phase is measured and not the integer number of cycles from satellite to the Earth's surface: the phase observations are "wrapped". The phase observations of neighboring PS candidates are filtered and those with the lowest residual noise are selected. Specifically, a band-pass filter consisting in an adaptive phase filter combined with a low-pass filter and applied in the frequency domain, is used. Each pixel is first weighted by setting the amplitude in all interferograms to an estimate of the signal-to-noise ratio (SNR) for the pixel, which in the first iteration is estimated from D_A. SNR is estimated using these residues in subsequent iterations. Once the algorithm has converged on estimates for the phase stability of each pixel, those most likely to be PS pixels are selected, with a threshold determined by the fraction of false positives deemed acceptable. Optionally, pixels that persist only in a subset of the interferograms and those that are dominated by scatterers in adjacent PS pixels may be rejected. A phase stability indicator, γ_x, is defined based on the temporal coherence and can be used to evaluate whether the pixel is a PS:

$$\gamma_x = \frac{1}{N} \left| \sum_{i=1}^{N} exp\left\{ j\left(\varphi_{int,x,i} - \overline{\varphi}_{int,x,i} - \Delta\hat{\varphi}_{h,x,i} \right) \right\} \right| \tag{4}$$

where N is the number of interferograms and $\Delta\hat{\varphi}_{h,x,i}$ is the estimate of the wrapped phase $\varphi_{int,x,i}$ of the xth pixel in the ith *flattened* and topographically corrected interferogram. After every iteration, the root-mean-square change in coherence, γ_x, determined as in Eq. (4) is calculated. When this ceases to decrease, the solution has converged and the algorithm stops iterating. Then pixels are selected based on the probability that they are PS pixels, considering their amplitude dispersion, as well as γ_x, (section 2 of Fig. 2). See Hooper et al.(2007) for details.

Once the PS has been selected, their phase is corrected for spatially-uncorrelated look angle (SULA) error (DEM error) by subtracting the estimated values. As long as the density of PS is such that the absolute phase difference between neighboring PSs,

Table 4
Mean coherence values obtained for (some) interferogram coregistered using the DePSI and the StaMPS coregistration implementations. The dashed rectangle highlights the interferograms with lower coherence.

Acquisition date	$B_\perp$ (m)	ΔT (days)	Mean coherence values					PSI method
			Crop1	Crop2	Crop3	Crop4	Crop5	
09-JAN-2000	−37	910	0.4655	0.5056	0.4735	0.4625	0.4612	DePSI
			0.4656	0.5056	0.4734	0.4625	0.4611	StaMPS
08-FEB-1998	−140	210	0.4647	0.4951	0.4709	0.4618	0.4591	DePSI
			0.4647	0.4951	0.4710	0.4617	0.4591	StaMPS
19-MAY-1996	198	−419	0.4571	0.4924	0.4658	0.4555	0.4508	DePSI
			0.4571	0.4925	0.4658	0.4554	0.4508	StaMPS
13-AUG-1995	207	−700	0.4598	0.4980	0.4705	0.4564	0.4533	DePSI
			0.4598	0.4980	0.4706	0.4564	0.4533	StaMPS
04-MAY-1997	−225	−70	0.4776	0.5057	0.4840	0.4792	0.4628	DePSI
			0.4777	0.5057	0.4841	0.4792	0.4629	StaMPS
31-DEC-1995	312	−559	0.4371	0.4588	0.4424	0.4377	0.4311	DePSI
			0.4372	0.4589	0.4425	0.4378	0.4312	StaMPS
30-MAR-1997	409	−105	0.4349	0.4600	0.4401	0.4348	0.4279	DePSI
			0.4352	0.4601	0.4403	0.4349	0.4280	StaMPS
15-OCT-2000	582	1190	0.3679	0.3827	0.3696	0.3685	0.3654	DePSI
			0.3684	0.3828	0.3697	0.3687	0.3656	StaMPS
28-JUN-1998	*−702*	*349*	*0.3688*	*0.3841*	*0.3690*	*0.3599*	*0.3767*	*DePSI*
			0.3695	*0.3842*	*0.3692*	*0.3603*	*0.3765*	*StaMPS*
02-DEC-1993	*919*	*−1319*	*0.2909*	*0.2806*	*0.2828*	*0.2790*	*0.3103*	*DePSI*
			0.2916	*0.3005*	*0.2921*	*0.2918*	*0.3005*	*StaMPS*
22-OCT-1995	*1029*	*−629*	*0.2954*	*0.2944*	*0.2873*	*0.2724*	*0.3210*	*DePSI*
			0.2955	*0.2992*	*0.2967*	*0.2905*	*0.3118*	*StaMPS*

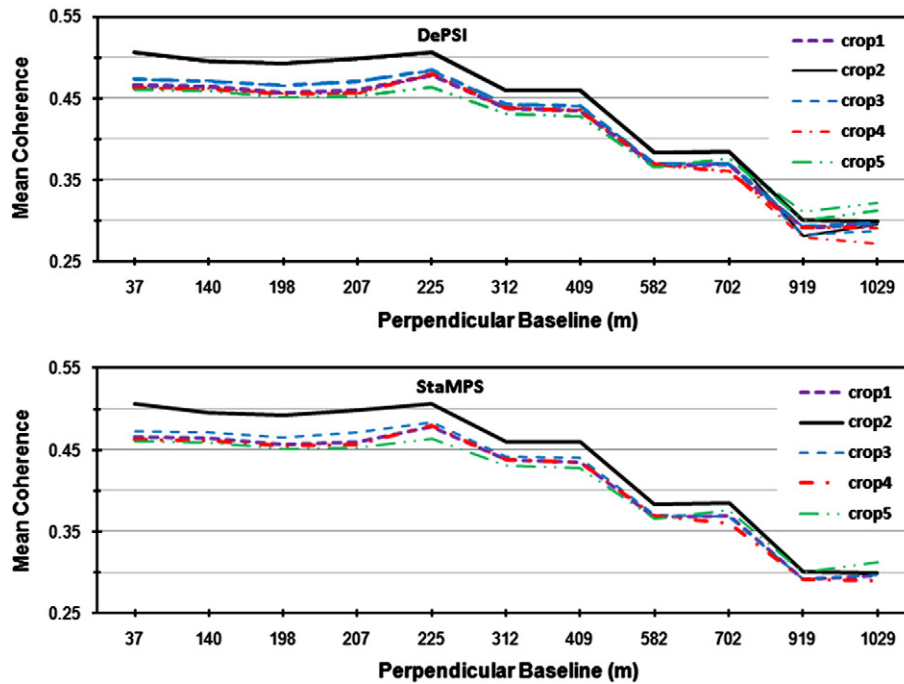Characters in italics are the interferograms with lower coherence.

Fig. 4. Graphic representation of the coherence values listed in Table. 4 as a function of the perpendicular baseline. The mean coherence decreases when $B_\perp$ increases. As expected, urban areas present the higher value of mean coherence and the mountainous areas the lowest regardless of the method applied.

after correction for estimated SULA error, is generally less than π, the corrected phase values can now be unwrapped.

The first "interpretable" PSI observation is the double-difference between master and slave for two nearby PS (Hanssen, 2004). The double-difference is both a temporal and a spatial difference. This implies that StaMPS also requires a spatial and a temporal reference: one acquisition time (master image) and one reference PS or reference area.

Optionally, after unwrapping, high-pass filtering can be applied to unwrapped data in time followed by a low-pass filter in space in order to remove the remaining spatial correlated errors (atmosphere and orbit errors).

Finally, subtracting this signal leaves essentially deformation and spatially uncorrelated errors which can be modeled as noise (section 3 of Fig. 2). All the remaining noise terms are supposed to be substantially reduced.

6. Comparative study

The main conceptual difference between DePSI and StaMPS lies in the deformation assumption. In DePSI pixels are selected based on the model of the temporal behavior while in StaMPS spatial smoothness of the deformation signal is assumed for PS selection. This can lead to different sets of PS being selected by each approach (Sousa et al., 2010a).

In the next sections, the most significant differences between both approaches are evaluated following the processing chain diagrams represented in Figs. 1 and 2. The preliminary results can be found in Sousa et al. (2010b).

6.1. Coregistration influence

In order to evaluate the influence of this step in both approaches, we computed the coherence between the master and the resampled
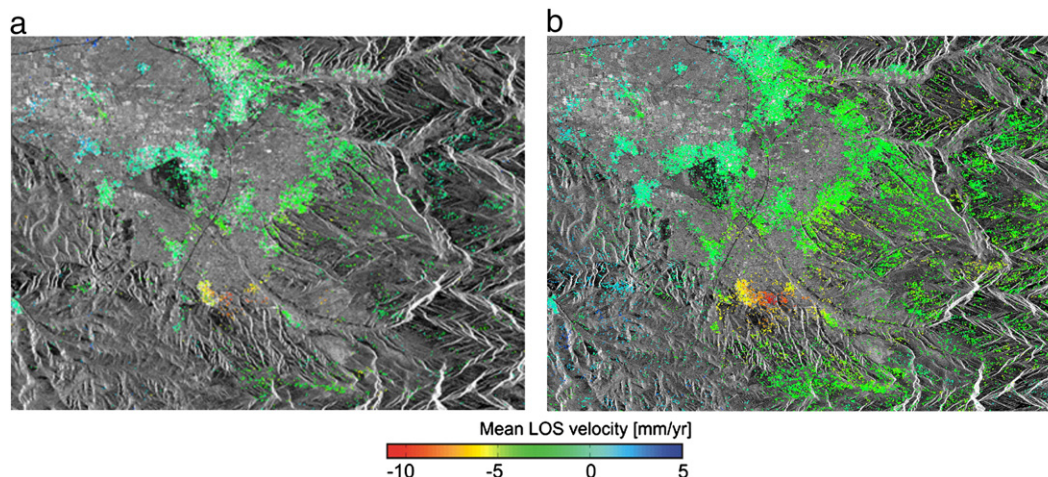

Fig. 5. StaMPS processing. (a) Without oversampling implementation; (b) with oversampling implementation (factor 2 in both azimuth and range directions). Although the deformation rates match it is clear that the amount of PS becomes much higher when oversampling is implemented.

Table 5
PS density as function of the soil occupation. Excluding the urbanized area which dominates the processed area the remaining area is characterized by agriculture fields with scattered farms, small villages and mountains. Crop locations and sizes are presented in Fig. 3.

PSI method	PS density per crop				
	Crop1	Crop2	Crop3	Crop4	Crop5
DePSI	55	355	120	27	0.5
StaMPS (no ovs)	18	55	23	10	12
StaMPS (ovs)	108	295	148	71	87

slave for different registration procedures. In other words, the coherence theory for SAR interferograms is employed (Cattabeni et al., 1994; Just & Bamler, 1994) to predict the effect of interpolation on the interferogram phase quality. The average of the whole coherence crop is used as criteria to evaluate the coregistration results of DePSI and StaMPS coregistration algorithms.

We divided the test area into different crops, covering distinct terrain occupations and processed each crop separately. Fig. 3 shows some crops used in the tests. As expected, the crops processed and presented in Fig. 3 have significant differences in coherence values depending on the type of the terrain they cover. The coherence along the mountain slopes is generally poor, mainly due to layover and shadow. Urban areas present high coherence due to the abundance of man-made constructions that behave as stable scatterers. The mean coherence values for some of the InSAR interferograms tested are included in Table 4 both using DePSI and StaMPS coregistration algorithms. Loss of coherence can be observed as function of the perpendicular baseline. For baselines close to 1000 m (~critical baseline) and even bigger, the urbanized areas appear with low coherence values. This effect is due to the geometric decorrelation caused by different observation geometries. These effects are confirmed in Fig. 4.

6.1.1. Discussion of the results

Both PSI approaches used in this work basically use the same method to coregister the SAR images with only one nuance: to avoid high geometrical decorrelation (and a corresponding low coherence) StaMPS uses a coregistration algorithm that applies an amplitude based method to estimate offsets in position between pairs of images with good correlation (only pairs with small perpendicular baseline are coregistered).
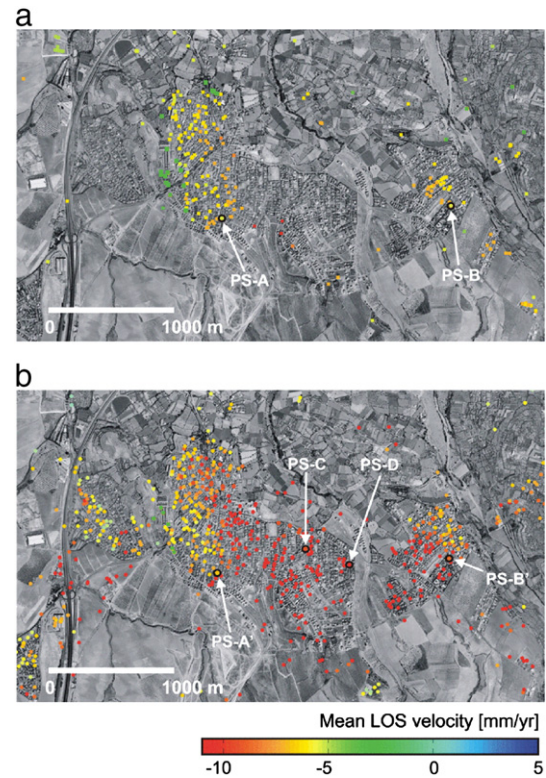

Fig. 7. PS distribution over Otura village returned by: (a) DePSI and (b) StaMPS. Some PSs are selected in each image inside the subsidence bowl and their time series are represented in Fig. 8. A 0.5 m resolution ortophoto is used as a background.

In order to verify the influence of these different methods, several tests have been performed and according to the main results obtained (see Table. 4) we can conclude that no significant difference between both approaches exists. In fact, when interferometric pairs with perpendicular baselines smaller than ~500 m, are used, the average coherence values obtained by both methodologies in areas with different varieties of coverage (urbanized, rural, and mountainous) are practically the same. For high perpendicular baseline values small differences of mean coherence values can be found which confirms better performance of StaMPS methodology.
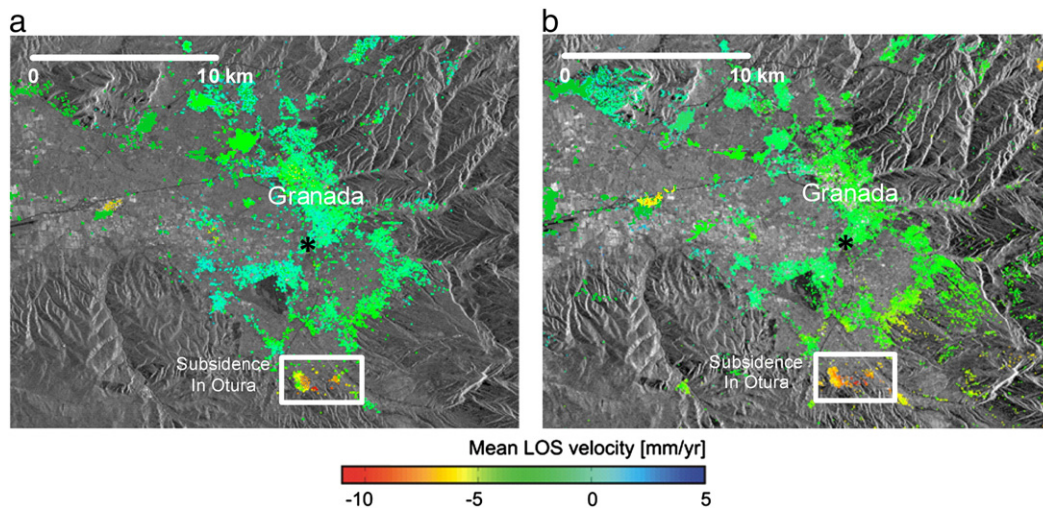

Fig. 6. ERS-1/2 stack PSI results of the whole area (corresponding to crop1 — Fig. 3) using: (a) DePSI; (b) StaMPS. A mean amplitude image is used as background. The reference point is indicated by the black asterisk. The areas marked with a small white box represent the highest deformation rates (Otura village) and are enlarged in Fig. 7.

In short, for this particular area, the coherence does not improve significantly as function of the methodology applied. This could be explained by the fact that the mean coherence values are always relatively high regardless of the crop used. In some particular cases, only the use of the StaMPS method allows the coregistration (Hooper, 2006).

Furthermore the processing time for the StaMPS coregistration method can be substantially higher, depending on the number of images used. For instance, for the Granada dataset composed by 29 scenes, 69 coregistrations are computed instead of the 28 required by the standard coregistration routine. Therefore, the coregistration methodology used by StaMPS only brings some benefits if the study area suffers from significant decorrelation.

6.2. Oversampling influence

In order to evaluate the oversampling effect, the results supplied by StaMPS processing with and without oversampling implementation are presented and compared. We implemented several tests in order to evaluate the oversampling influence on the final results. The StaMPS procedure was first applied with no oversampling implemented and the results were compared with DePSI. Then the oversampling step was implemented in the StaMPS processing chain and the results were compared with those previously obtained.

As presented in Sousa et al. (2010a), the density and the location of the PS appear to be the most obvious differences between both approaches. This fact could be related to the deformation behavior. Here we assess whether the oversampling implementation could be also a contributing factor.

Fig. 5 shows the results for the same area (Granada area, Spain) with and without oversampling implementation. The amount of PS is considerably higher when oversampling by a factor of 2 in both azimuth and range is applied. In total, 7256 PSs were detected without oversampling compared to 44.189 PSs when oversampling is included. Apparently, oversampling results in 6 times more PSs which can be very significant.

6.2.1. Discussion of the results

The average PS density in the area of interest depends on the PSI methodology used. With DePSI the total area is covered by ~55 PS/km^2. This compares to 18 PS/km^2 when the standard StaMPS configuration is used. However, if oversampling is implemented in the StaMPS processing this number increases to more than 100 PS/Km^2. These PSs are not evenly distributed. The PS density varies from up to 0–10 PS/km^2 in the rural/mountain areas to over 100 PS/km^2 in the urbanized areas (Table. 5). The picture is drastically different in the case of StaMPS. In general, the PS density in urbanized areas is lower than it is in DePSI (standard processing); however, the density is significantly increased in the rural and mountain areas, which constitutes the main advantage of StaMPS (See Table. 5). If oversampling is implemented in the StaMPS processing chain, the PS density increases so that the density in the urbanized areas is similar to the results provided by DePSI but in all the remaining covers the density is significantly higher. Fig. 6 illustrates this effect more clearly. It is clear that DePSI detects much fewer PS in the center of the subsidence bowl (Fig. 7a) when compared with StaMPS (Fig. 7b).

In Fig. 8, time series plots, for four PSs located inside the subsidence area, are shown (position of the PS points given in Fig. 7). DePSI PS time series are quite linear as expected due to the linear assumption used. PS time series of the points only selected by StaMPS (PS-C and PS-D), despite the linear behavior shown, present a
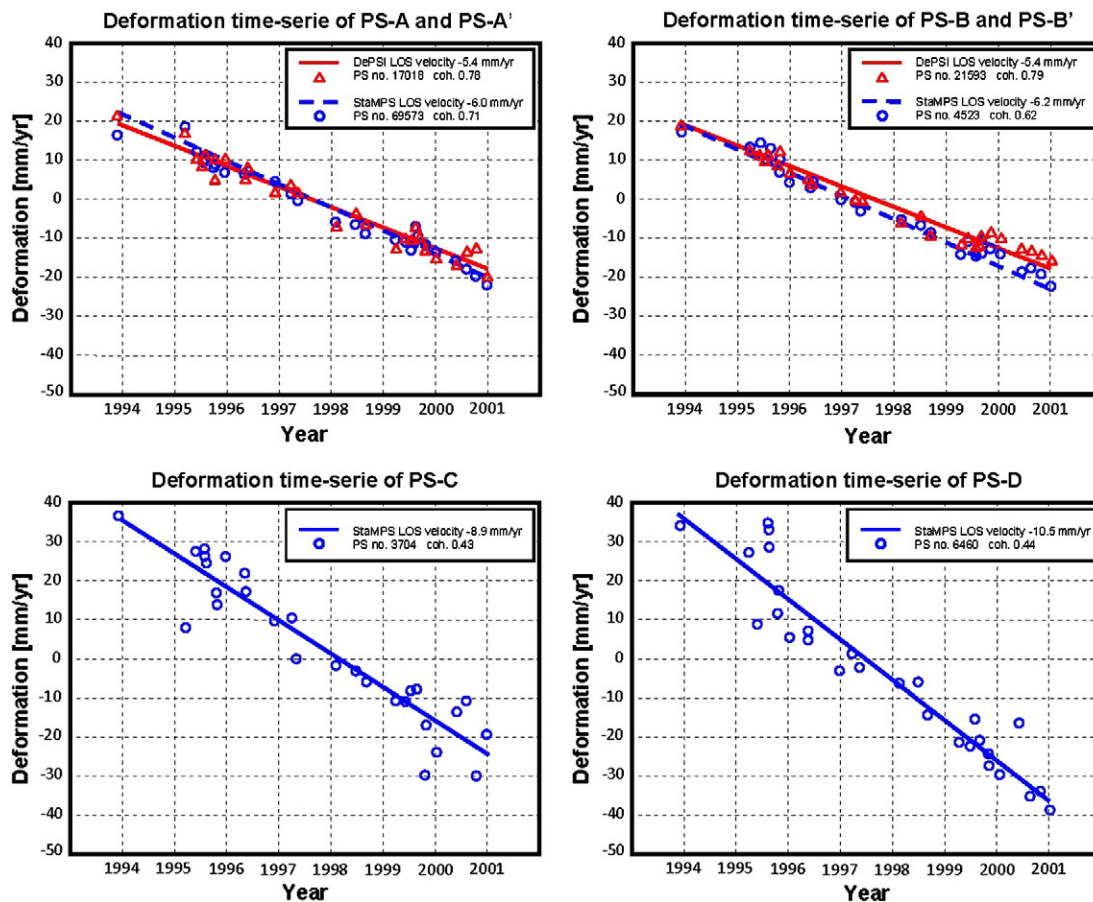

Fig. 8. Displacement time series of the selected PS in Fig. 7 with respect to the reference point (represented in Fig. 6). PS-A and PS-B are returned by DePSI and PS-A', PS-B', PS-C and PS-D by StaMPS. PS-A and PS-A', and PS-B and PS-B' are located in nearby positions respectively.

Table 6
Line-of-Sight (LOS) displacement rates estimated with DePSI and StaMPS of the two common PS given in Fig. 7.

PS	Latitude	Longitude	DePSI		StaMPS		vel^{DePSI}-vel^{StaMPS}
			Vel (mm/yr)	Coh	Vel (mm/yr)	Coh	(mm/yr)
A	37°.08574	−3°.63459	−5.4	0.78	−6.0	0.71	+0.6
B	37°.08676	−3°.61662	−5.4	0.79	−6.2	0.62	+0.8

high level of noise. This may be the explanation to the fact that they were not selected by DePSI.

The estimated displacement rates and the quality of the compared PSs (A–A' and B–B') are listed in Table 6, for both DePSI and StaMPS. The bias between algorithms for both estimates may be partly due to the fact that in DePSI, velocities are with respect to a specific PS, whereas in StaMPS they are with respect to all PSs within a specified radius (3 km in this case).

The increase in the PS number after oversampling is expected mainly due to dominant scatterers that are not located in the center of the original resolution cell. However, these "new PSs" should be, in fact, influenced by the one in the adjacent pixel. A scatterer that is bright can dominate pixels other than the pixel corresponding to its physical location. The error in look angle and squint angle due to the offset of the pixel from the physical location usually results in these pixels not being selected as PS. However, the slight oversampling of the resolution cells can cause pixels immediately adjacent to the PS pixel to be dominated by the same scatterer where the error may be sufficiently small that the pixel appears stable. To avoid picking these pixels, we assume that adjacent pixels selected as PS are due to the same dominant scatterer. As we expect the pixel that corresponds to the physical location to have the highest SNR, for groups of adjacent stable pixels we select as the PS only the pixel with the highest value of coherence.

We specifically exclude pixels that could be dominated by the same scatterer, by searching for clusters of adjacent pixels, and keeping only the pixel with the highest coherence. When the data are oversampled, the window used for coherence computation is also increased by a factor of two in both directions and oversampling during coregistration is reduced by a factor of 2 resulting in the same coregistration accuracy.

Fig. 9 presents the overlapped histograms relative to the coherence values considering all PSs obtained with oversampling and only the extra PS obtained by resampling. There is not a significant degradation of the coherence, implying that the increase in the number of PS was not achieved due to the inclusion of PS with noisier phase.

The improvement in the PS location is another benefit expected by applying oversampling because the radar coordinates of an over-sampled image are at sub-pixel level with respect to the original sampling rate.

Motivated by these results, a similar test was realized (Arikan et al., 2010) in the West Anatolia area, Turkey. This region is rural and only few PSs can be detected when StaMPS standard design is applied. However, when oversampling is implemented the results are significantly improved, 417 PSs were detected before applying oversampling in the StaMPS processing chain against 2029 PSs after oversampling implementation.

We propose two reasons why the number of PS would increase. First, in the case where a dominant scatterer is close to the edge of a resolution cell, its influence is downweighted by the appropriate value of a sync function centered on the middle of the cell. In a neighboring (overlapping) oversampled resolution cell, this scatterer would lie close to the center and hence have a higher weight, leading to increased SNR. Second, when two dominant scatterers lie close to each other they may both influence a resolution cell, which would not then behave as a PS. Neighboring oversampled resolution cells may be dominated by only one of the scatterers leading them to behave as PS.

Fig. 10 shows a comparison of Mean LOS Velocity (MLV) for homologous pixels (PS) selected by both methods. This picture allows a quantitative comparison between PS motion (MLV [mm/yr]) computed by means of DePSI and StaMPS. For assessment of the similarity between DePSI and StaMPS deformation velocities the correlation coefficient was computed and having been found the value of 0.8997, which indicates a strong correlation between both methodologies.

6.3. Influence of PS selection methodologies

In order to test the influence of the different approaches in the PS selection, we used a SAR dataset with particular characteristics. A controlled corner reflector experiment has been set up with leveling as an independent validation technique (Marinkovic et al., 2007). Since early 2003, during almost five years, the movements of five corner reflectors in the area near Delft University of Technology were monitored using leveling and repeat-pass InSAR (ERS-2 and Envisat).

According to the way that DePSI selects PS, very bright points with a very stable phase in time located in an area undergoing slow deformation will be selected as PS. But the question rises: *Will StaMPS be able to detect these points as PS?*

In the first stage, when StaMPS selects PS candidates based on amplitude dispersion, these points will be selected as well due to its
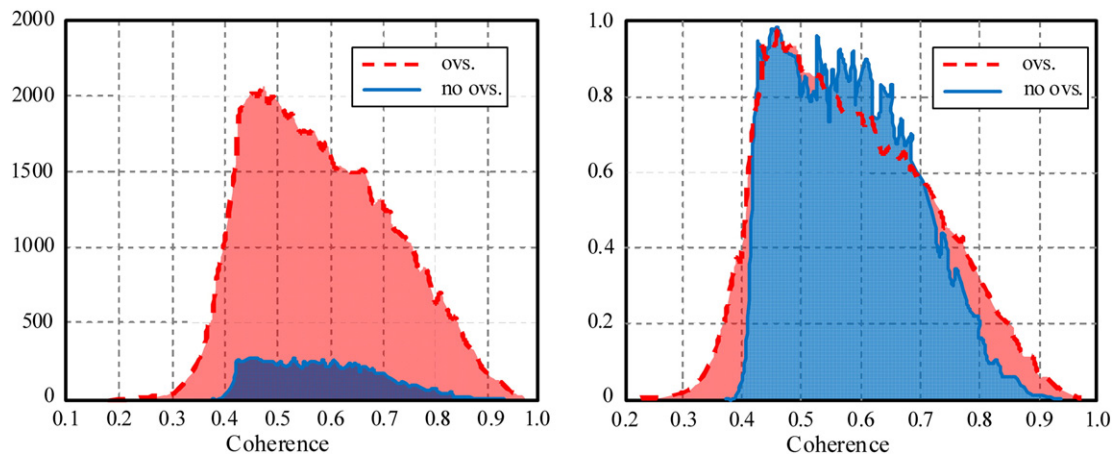

Fig. 9. Coherence density distribution using all the PS obtained from the processing of the area related to Fig. 6. (left) Absolute histogram; (right) normalized histogram. Few noisy points have been added to the selection (coh<0.4) however this number is negligible when compared to the quality of the majority of the new points.
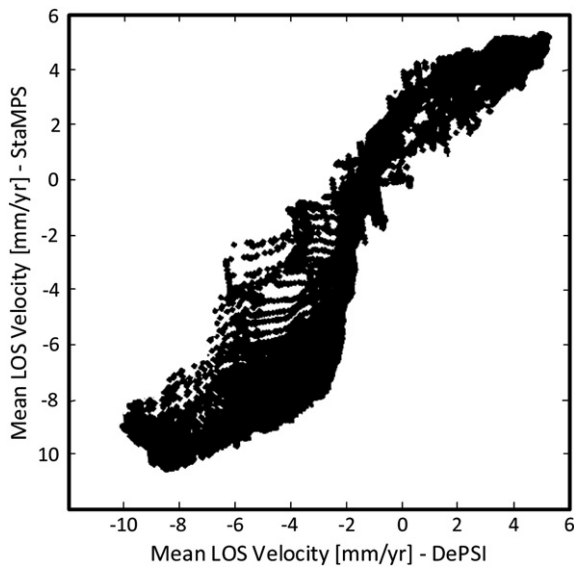
Fig. 10. Comparison of mean LOS velocity for all homologous PSs in the area corresponding to Fig. 6.

7. Conclusion

We have investigated the most significant differences in the StaMPS and DePSI processing chains in order to depict the behavior of each PSI approach according to the area and to the deformation regime. Critical differences in the interferometric processing were studied: SAR image coregistration and oversampling. It was confirmed that StaMPS coregistration method has benefits; however, these improvements are not significant in the case where the study area maintains a reasonable correlation, even if long perpendicular baselines are used. Another significant difference in the interferometric processing regards the oversampling step. StaMPS, unlike DePSI, does not includes this step in its standard design. The benefits from the inclusion of the oversampling step in StaMPS were evaluated and the results demonstrated that significant improvements, mainly in the PS density, are obtained. Because of this, oversampling has been added to StaMPS framework as default option in the latest release.

Secondly, the PS processing part of each methodology was analyzed and evaluated. We concluded that StaMPS and DePSI are complementary in different aspects like the case of PS selection and unwrapping which can be used to improve the results.

Despite these differences, some of them significant, the general deformation framework has been detected by both approaches when applied to different datasets.

The next step in the development of this project will be the integration of the major advantages of both PSI approaches because the expected benefits will be considerable mainly in the areas where man-made structures are scarce.

very stable phase response. Then, candidates are filtered in small patches to determine the spatially-correlated phase. This is an iterative procedure that estimates the phase noise of each candidate in every interferogram. Noisy pixels are downweighted in the filtering and iteration continues until convergence of phase noise estimates is achieved. According to this principle, the corner reflectors will be detectable by StaMPS if there are candidate pixels in the surrounding patch that maintain some coherence, and the difference in motion between the reflectors and the background is not too great. In that case these movements will be considered as noise. In Fig. 11, the results provided by both approaches can be compared. The general results are very similar both in density and in the relative deformations estimated. Same results and relative deformations are also derived inside the region of the corner reflectors.
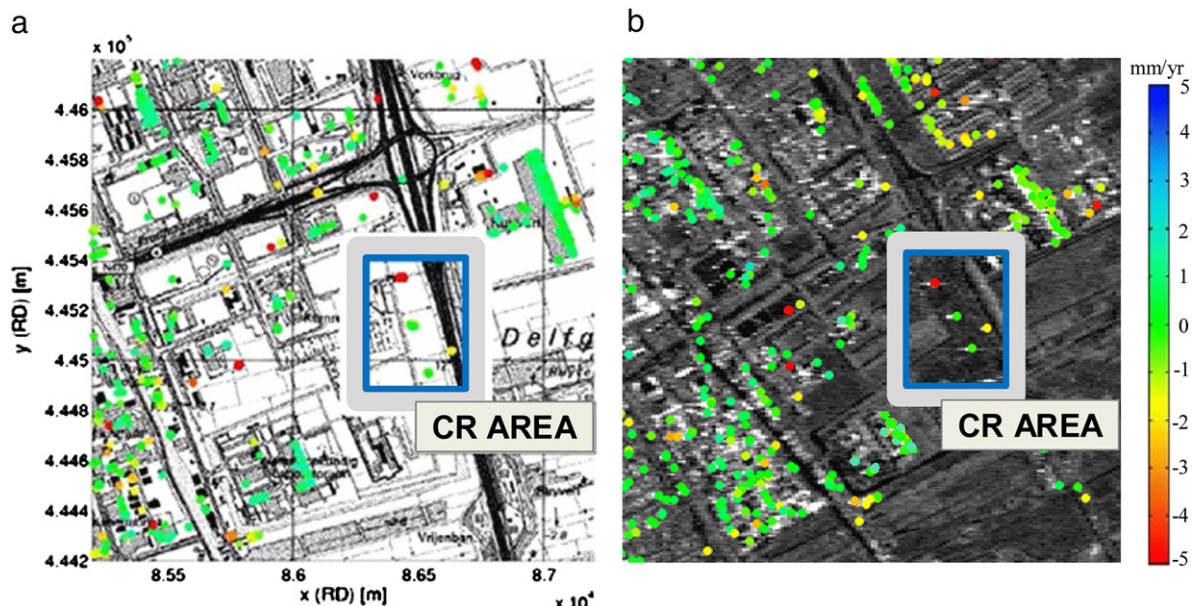

Fig. 11. Linear velocities in the corner reflectors area provided by: (a) DePSI. A topographic map is used as background (Marinkovic et al., 2007); (b) StaMPS results superimposed to a SAR amplitude image. It is possible to check the similarity between the linear velocities.

References

Arikan, M., Hooper, A., & Hanssen, R. (2010). Radar time series analysis over west anatolia. : European Space Agency (Special Publication) ESA SP-677, 2010.

Bamler, R., & Hartl, P. (1998). Synthetic aperture radar interferometry. *Inverse Problems*, *14*, R1–R54.

Burgmann, R., Schmidt, D., Nadeau, R. M., d'Alessio, M., Fielding, E. J., Manaker, D., et al. (2000). Earthquake potential along the Northern Hayward Fault, California. *Science*, *289*, 1178–1182.

Cattabeni, M., Monti-Guarnieri, A., & Rocca, F. (1994). Estimation and improvement of coherence in SAR interferograms. *Proceedings of IGARSS 94, Pasadena, California.*

Doornbos, E., & Scharro, R. (2004). *Improved ERS and Envisat precise orbit determination.* Proceedings of ERS/Envisat Symposium Saltzburg 2004. The orbit files are available at http://www.deos.tudelft.nl/ers/precorbs/orbits/

Ferretti, A., Prati, C., & Roca, F. (1999). Multibaseline InSAR DEM reconstruction: The wavelet approach. *IEEE Transactions on Geoscience and Remote Sensing, 37*(2), 705–715.

Ferretti, A., Prati, C., & Rocca, F. (2000). Nonlinear subsidence rate estimation using permanent scatters in differential SAR interferometry. *IEEE Transactions on Geoscience and Remote Sensing, 38*(5), 2202–2212.

Ferretti, A., Prati, C., & Rocca, F. (2001). Permanent scatters in SAR interferometry. *IEEE Transactions on Geoscience and Remote Sensing, 39*(1), 8–20.

Galindo-Zaldívar, J., González-Lodeiro, F., & Jabaloy, A. (1993). Stress and palaeostress in the Betic-Rif cordilleras (Miocene to the present). *Tectonophysics, 227*, 105–126.

Hanssen, R. F. (2001). Radar interferometry: Data interpretation and error analysis. Dordrecht: Kluwer Academic Publishers 2001.

Hanssen, R. F. (2004). Stochastic modeling of times series radar interferometry. *International Geoscience and Remote Sensing Symposium, Anchorage, Alaska, 20–24 September 2004.*

Hooper, A. (2006). Persistent Scaterrer Radar Interferometry for Crustal Deformation Studies and Modeling of Volcanic Deformation. PhD thesis.

Hooper, A., Segall, P., & Zebker, H. (2007). Persistent scatterer InSAR for crustal deformation analysis, with application to Volcán Alcedo, Galapagos. *Journal of Gephysical Research, 112*, B07407. doi:10.1029/2006JB004763.

Hooper, A., Zebker, H., Segall, P., & Kampes, B. (2004). A new method for measuring deformation on volcanoes and other natural terrains using InSAR persistent scatterers. *Geophysical Research Letters, 31*, L23611. doi:10.1029/2004GL021737, 2004.

Just, D., & Bamler, R. (1994). Phase statistics of interferograms with applications to synthetic aperture radar. *Applied Optics, 33*(20), 4361–4368.

Kampes, B. M. (2005). Radar interferometry: Persistent scatterer technique. Dordrecht, The Netherlands: Kluwer Academic Publishers.

Kampes, B. M., & Usai, S. (1999). Doris: the Delft Object-oriented radar interferometric software, 2nd International Symposium on Operationalization of Remote Sensing. The Netherlands: Enschede.

Ketelaar, V.B.H., 2008. Monitoring surface deformation induced by hydrocarbon production using satellite radar interferometry. PhD thesis, Delft University of Technology, Delft, The Netherlands.

Leijen, F. J. V., & Hanssen, R. F. (2007). Persistent Scatterer interferometry using adaptive deformation models. *ESA ENVISAT Symposium, Montreux, Switzerland, 23–27 April 2007* 6 pp., CD-ROM ESA SP-636.

Marinkovic, P., Ketelaar, G., van Leijen, F., & Hanssen, R. (2007). InSAR quality control: Analysis of five years of corner reflectors time series. *Fringe Workshop 2007. Frascati, 26–30 November 2007, Italy.*

Sanz de Galdeano, C., & Vera, J. A. (1992). Stratigraphic record and palaeogeographical context of the Neogene basins in the Betic Cordillera. *Spain Basin Research, 4*, 21–36.

Scharroo, R., & Visser, P. (1998). Precise orbit determination and gravity field improvement for the ERS satellites. *Journal of Geophysical Research, 103*(C4), 8113–8127.

Sousa, J.J. (2009). Potential of Integrating PSI Methodologies in the Detection of Surface Deformation. PhD Thesis, University of Porto, Portugal.

Sousa, J. J., Hooper, A., Hanssen, R. F., & Bastos, L. (2010). Comparative study of two different PS-InSAR approaches: DePSI vs. StaMPS. *Proceedings of FRINGE 2009 Workshop, Frascati, 2009.*

Sousa, J. J., Ruiz, A. M., Hanssen, R. F., Bastos, L., Gil, A., Galindo-Zaldívar, J., et al. (2010). PSI processing methodologies in the detection of field surface deformation—Study of the Granada basin (Central Betic Cordilleras, southern Spain). *Journal of Geodynamics.* doi: 10.1016/j.jog.2009.12.002.

Suchandt, S., Breit, H., Adam, N., Eineder, M., Schättler, B., Runge, H., et al. (2001). The shuttle radar topography mission. *High Resolution Mapping from Space 2001, Hannover, 2001. Joint Workshop of ISPRS Working Groups I/2, I/5 and IV/7. Hannover: ISPRS, 2001* (pp. 235–242). 1 CD-ROM.

Usai, S. (1997). The use of man-made features for long time scale INSAR. Geoscience and Remote Sensing, 1997. *IGARSS '97. Remote sensing — A scientific vision for sustainable development, 1997. IEEE International, 4.* (pp. 1542–1544).

Usai, S., & Hanssen, R. (1997). Long time scale INSAR by means of high coherence features. *3rd ERS Symposium on Space at the service of our Environment, Florence, Italy, 14–21 March, European Space Agency.*

van der Kooij, M., Hughes, W., Sato, S., & Poncos, V. (2006). Coherent target monitoring at high spatial density: Examples of validation results. *Eur. Space Agency Spec. Publ., SP-610.*

Zebker, H. A., & Villasenor, J. (1992). Decorrelation in interferometric radar echoes. *IEEE Transactions on Geoscience and Remote Sensing, 30*(5), 950–959.